International Journal of Heat and Mass Transfer 151 (2020) 119385

Contents lists available at ScienceDirect

International Journal of Heat and Mass Transfer

journal homepage: www.elsevier.com/locate/hmt

Melting heat transfer of power-law non-Newtonian phase change nano-enhanced n-octadecane-mesoporous silica (MPSiO$_2$)

S.A.M. Mehryan[a], Mohammad Vaezi[b], Mikhail Sheremet[c], Mohammad Ghalambaz[d,e,*]

[a] *Young Researchers and Elite Club, Yasooj Branch, Islamic Azad University, Yasooj, Iran*
[b] *Faculty of mechanical engineering, K. N. Toosi University of Technology, Tehran, Iran*
[c] *Laboratory on Convective Heat and Mass Transfer, Tomsk State University, Tomsk, Russia*
[d] *Department for Management of Science and Technology Development, Ton Duc Thang University, Ho Chi Minh City, Vietnam*
[e] *Faculty of Applied Sciences, Ton Duc Thang University, Ho Chi Minh City, Vietnam*

ARTICLE INFO

Article history:
Received 17 October 2019
Revised 4 January 2020
Accepted 13 January 2020
Available online 7 February 2020

Keywords:
Phase change material
Power-law model
Nanoparticles
Melting process
Deformed mesh technique

ABSTRACT

The heat transfer removal from heated elements in different engineering devices is the main challenge for each engineer in various fields. This problem can be solved using an effective heat-transfer agent or by increasing the heat transfer surface. The present work is devoted to an opportunity to use the phase change material with nanoparticles for an intensification of heat removal within a gap between two coaxial vertical isothermal cylinders. The analysis was performed numerically using the Galerkin finite element approach in the case of the non-Newtonian nature of the nano-enhanced PCM. The power-law was used for the description of the non-Newtonian behavior of the considered material. For the solution to the Stefan problem, a deformed mesh method, based on the Arbitrary Lagrangian–Eulerian (ALE), was used. The developed computational code was validated using the numerical and experimental data of other authors. The effects of the nanoparticles volume fraction, aspect ratio and Fourier number on the melting process were investigated. It has been revealed that the inclusion of nanoparticles within the phase change material leads to both less intensive melting of the material and a reduction of the average Nusselt number.

1. Introduction

The development of different engineering applications demands the creation of effective heat removal techniques from heated elements or effective thermal storage systems. Nowadays, research within the considered fields is based on the application of phase change materials [1–6] that have a moderate melting temperature, high heat capacity, and high latent phase change energy. Moreover, the melting or solidification process occurs with constant phase change temperature.

There are many published theoretical and experimental papers [7–12] illustrating the behavior of PCM and the opportunities to use these materials for the improvement of various engineering devices. Thus, Jiang et al. [7] experimentally studied cylindrical battery thermal management using the copper foam-PCM composite. It was ascertained that the thermoelectric cooling technique could be more effective in comparison with natural convection and liquid cooling. CFD analysis of the gallium melting process within a cylindrical cavity with four heat sources was performed by Bouhal et al. [8]. The authors showed that the inclusion of fins allowed intensifying the melting process due to the extended surface of the heat transfer. A numerical study of phase changes in a single tank filled with PCM capsules was conducted by Lee et al. [9]. An optimal arrangement of cooling-PCM and heating-PCM was found. Bechiri and Mansouri [10] numerically investigated the melting of phase change material within a vertical cylindrical tube taking into account the volumetric expansion. Calculations were performed using the finite volume method. The conducted parametric study showed that the Stefan number influence on the melting process is essential for a higher outer wall temperature.

Numerical and experimental analysis of the heat pipe module filled with phase change material was conducted by Behi et al. [11]. Authors demonstrated that the PCM-assisted heat pipe allows obtaining at about 87% of the required cooling load in the case of the power range between 50 and 80 W. Such a result can be used for more effective cooling of electronic devices. Iachachene et al. [12] numerically examined PCM melting heat transfer within a trapezoidal cavity under the impact of cavity orientation and nanoparticle inclusion. Calculations were performed using the

---

* Corresponding author.
E-mail address: mohammad.ghalambaz@tdtu.edu.vn (M. Ghalambaz).

https://doi.org/10.1016/j.ijheatmasstransfer.2020.119385
0017-9310/© 2020 Elsevier Ltd. All rights reserved.

Nomenclature

Cp	heat capacity at constant pressure
$\vec{g}$	gravity acceleration
L_h	latent heat
m	consistency of dynamic viscosity
n	power-law index of the non-Newtonian fluid
p	dimensional pressure
P	non-dimensional pressure
s	solid PCM
t	dimensional time
T	Temperature
tr	Transpose of the matrix
Greek symbols	
ρ	Density
β	thermal expansion coefficient
μ	dynamic viscosity
ϕ	volume fraction
ϕ_{wt}	mass fraction
Subscripts	
c	Cold
f	Fluid
fu	fusion temperature
h	Hot
nf	nano-PCM at fluid phase
np	Nanoparticles
ns	nano-PCM at the solid phase
wt	weight quantity

enthalpy-porosity technique on the basis of the FLUENT software. The addition of nanoparticles leads to a non-monotonic variation of the melting rate. Ghalambaz et al. [13] calculated melting energy transport in a square differentially heated chamber under the impact of a magnetic source. The effects of the Hartmann number and magnetic source location on liquid flow and thermal transmission were investigated. The authors demonstrated the appearance of a uniform phase change line under the influence of the magnetic field. Three-dimensional and two-dimensional simulation of the melting process within cavities filled with phase change materials was performed by Bondareva and Sheremet [14–18] using the computational codes developed on the basis of the non-primitive variables. Obtained results characterize an opportunity to enhance the heat removal from the local heat sources.

The heat transfer improvement can be achieved by an introduction of nanoparticles of low concentration [19–25]. Such solid particles can be added also to phase change materials [26–32]. Thus, Ghalambaz et al. [26] numerically investigated natural convection melting of hybrid nanofluids within a differentially heated cavity with various values of nanoparticles volume fraction, conductivity and viscosity parameters. The authors found that the conductivity parameter has an essential influence on the liquid fraction in comparison with the viscosity parameter. Extension of [26] to the case of the heated internal cylinder and cooling from the cavity walls was done by Chamkha et al. [27]. The authors performed computational analysis using the Galerkin finite element method. It was revealed that the phase change line is affected significantly by the nanoparticles volume fraction for high thermal conductivity. Other interesting results on nano-encapsulated phase change materials behavior can be found in [28,29].

The objective of the present study is a numerical analysis of nano-enhanced n-octadecane melting heat transfer within a gap between coaxial isothermal vertical cylinders in the case of non-Newtonian behavior of the considered material. The analyzed problem has many engineering applications related to more effective heat removal from the heated pipes for heat exchangers or in the case of the creation of comfortable conditions within the building elements with cylindrical encapsulated PCM elements.

2. Physics of the problem and formulation

One coaxial pipe having the aspect ratio of AR is the domain of interest for this work, as schematically illustrated in Fig. 1. Herein, the aspect ratio is the ratio of the height of the coaxial pipe to the difference between the outer and inner radiuses (i.e. $AR = H/(r_o - r_i)$). The inner pipe of radius r_i is held at a higher temperature of $T_h = 318$ K While the outer pipe of radius r_o is cold with a lower temperature of $T_c = 298$ K. The upper and lower walls of the enclosure are adiabatic through an insulating material. The void space between the inner and outer cylindrical surfaces is fully filled by the n-octadecane containing mesoporous silica (MPSiO$_2$) nanoparticles. The melted n-octadecane with the MPSiO$_2$ nanoparticles can act as a power-law non-Newtonian fluid. The volume change of the mixture during the melting process is considered to be zero. Also, the Boussinesq approximation is considered to be established to model the buoyancy force. The equations modeling the thermal and dynamic behavior of a laminar, non-Newtonian, unsteady and incompressible flow are:

Continuity equation [33]:

$$\frac{1}{r}\frac{\partial (r u_r)}{\partial r} + \frac{\partial u_z}{\partial z} = 0 \tag{1}$$

Momentum equation [11,33]:

$$\rho_{NP}\left[\frac{\partial u_r}{\partial t} + u_r\frac{\partial u_r}{\partial r} + u_z\frac{\partial u_r}{\partial z}\right] = -\frac{\partial p}{\partial r} + \frac{1}{r}\frac{\partial}{\partial r}\left(2\mu_{nf} r\frac{\partial u_r}{\partial r}\right) - \frac{2\mu_{nf} u_r}{r^2} + \frac{\partial}{\partial z}\left(\mu_{nf}\left(\frac{\partial u_r}{\partial z} + \frac{\partial u_z}{\partial r}\right)\right) \tag{2a}$$

$$\rho_{NP}\left[\frac{\partial u_z}{\partial t} + u_r\frac{\partial u_z}{\partial r} + u_z\frac{\partial u_z}{\partial z}\right] = -\frac{\partial p}{\partial z} + \frac{1}{r}\frac{\partial}{\partial r}\left(\mu_{nf} r\left(\frac{\partial u_r}{\partial z} + \frac{\partial u_z}{\partial r}\right)\right) + \frac{\partial}{\partial z}\left(2\mu_{nf}\frac{\partial u_z}{\partial z}\right) + \rho_{NP} g\beta_{nf}(T_{nf} - T_{fu}) \tag{2b}$$

where

$$\mu_{nf}(\dot{\gamma}) = m_{nf}\dot{\gamma}^{n_{nf}-1} | \dot{\gamma} = 2\left[\left(\frac{\partial u_r}{\partial r}\right)^2 + \left(\frac{u_r}{r}\right)^2 + \left(\frac{\partial u_z}{\partial z}\right)^2\right] + \left(\frac{\partial u_r}{\partial z} + \frac{\partial u_z}{\partial r}\right)^2 + \left(\frac{\partial u_z}{\partial r}\right)^2 \tag{3}$$

The subscript of NP denotes the averaged properties of nano-PCM. However, nf defines the properties of melted nano-PCM. Energy conservation equation for the fluid subregion [11,33]:

$$\rho_{NP} C_{p,nf}\left[\frac{\partial T_{nf}}{\partial t} + u_r\frac{\partial T_{nf}}{\partial r} + u_z\frac{\partial T_{nf}}{\partial z}\right] = \frac{1}{r}\frac{\partial}{\partial r}\left(k_{nf} r\frac{\partial T_{nf}}{\partial r}\right) + \frac{\partial}{\partial z}\left(k_{nf}\frac{\partial T_{nf}}{\partial z}\right) \tag{4}$$

Energy conservation equation for the solid subregion:

$$\rho_{NP} C_{p,ns}\frac{\partial T_{ns}}{\partial t} = \frac{1}{r}\frac{\partial}{\partial r}\left(k_{ns} r\frac{\partial T_{ns}}{\partial r}\right) + \frac{\partial}{\partial z}\left(k_{ns}\frac{\partial T_{ns}}{\partial z}\right) \tag{5}$$

ns subscript of the above equations describes the solid nano-PCM. Applying the energy balance on the forwarding interface boundary results in the following relations [13]:

$$u_r = \frac{k_{nf}\frac{\partial T_{nf}}{\partial r} - k_{ns}\frac{\partial T_{ns}}{\partial r}}{(\rho L_h)_{NP}} \tag{6a}$$

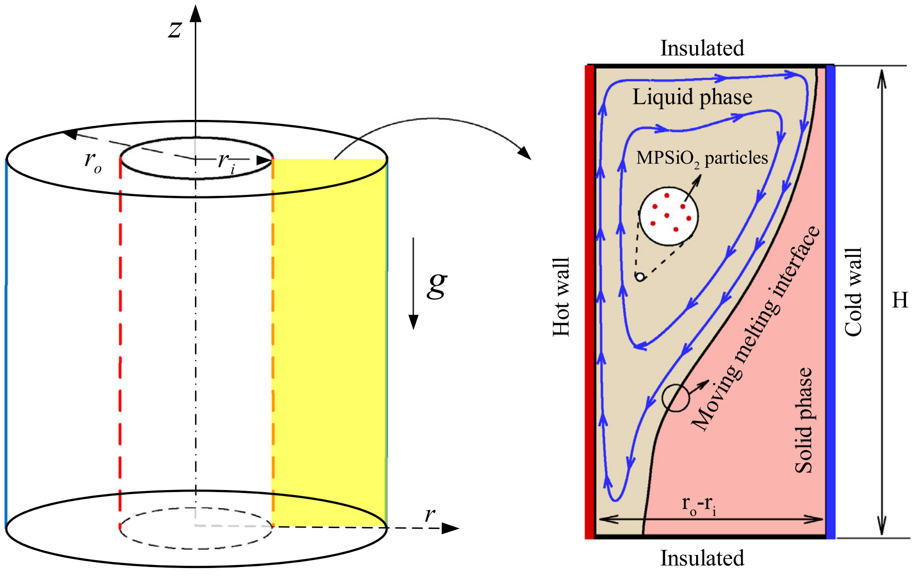

(a): 3D (b): 2D

Fig. 1. Schematic representation of the problem physics

Table 1
Thermal conductivity and correlated parameters for the viscosity of PCM containing MPSiO$_2$ particles [30].

Mass fraction (ϕ_{wt}) [%]	0.0	0.01	0.03	0.05
Volume fraction (ϕ) [%]	0.0	0.208	0.633	1.070
Power law index (n)	1.00	1.00	0.879	0.822
Consistency (m) [mPa.s^n]	3.536	3.987	7.910	11.021
Solid thermal conductivity (k_{ns}) [W/m.K]	0.371	0.375	0.383	0.381
Liquid thermal conductivity (k_{nf}) [W/m.K]	0.152	0.154	0.157	0.159

Table 2
Thermo-physical properties of the PCM and nanoparticles [35,36].

Properties of materials	n-octadecane	Silica nanoparticles
Density (solid/liquid) [kg/m^3]	865/ 770	3970
Thermal expansion coefficient [1/K]	9.1×10^{-4}	0.63×10^{-5}
Latent heat of fusion [kJ/kg]	243.5	–
Specific heat capacity (solid/ liquid) [J/kg.K]	1934/ 2196	765

$$u_z = \frac{k_{nf}\frac{\partial T_{nf}}{\partial z} - k_{ns}\frac{\partial T_{ns}}{\partial z}}{(\rho L_h)_{NP}} \tag{6b}$$

The temperature of the melting interface is fixed at the fusion temperature. As the temperature of the interface is fixed by the fusion temperature, the difference of heat fluxes from the right side of the interface (solid region) and the left side of the interface (liquid region) is consumed as the phase change in the form of latent heat. This condition, which is based on the surface energy balance, is known as the Stefan condition.

The governing equations are solved under the following boundary and initial conditions:

$$T = T_h,\ \ u_r = u_z = 0\ \ \forall r,\ z,\ t \mid r = r_i,\ \ 0 \le z \le H,\ \ t \ge 0 \tag{7a}$$

$$T = T_c,\ \ u_r = u_z = 0\ \ \forall r,\ z,\ t \mid r = r_o,\ \ 0 \le z \le H,\ \ t \ge 0 \tag{7b}$$

$$\frac{\partial T}{\partial z} = 0,\ \ u_r = u_z = 0\ \ \forall r,\ z,\ t \mid z = 0,\ \ r_i \le r \le r_o,\ \ t \ge 0 \tag{7c}$$

$$\frac{\partial T}{\partial z} = 0,\ \ u_r = u_z = 0\ \ \forall r,\ z,\ t \mid z = H,\ \ r_i \le r \le r_o,\ \ t \ge 0 \tag{7d}$$

$$T = T_0,\ \ u_r = u_z = 0\ \ \forall r,\ z,\ t \mid r_i \le r \le r_o,\ \ 0 \le z \le H,\ \ t = 0 \tag{7e}$$

At the fusion interface, the temperature is the fusion temperature as T_{fu} about 300.5 K [30], and the fluid velocity is the interface velocity. Moreover, the temperature of the cold wall and the initial temperature are the same, i.e., $T_0 = T_c$.

Since there is no model to give the thermal conductivity and parameters of dynamic viscosity of the non-Newtonian nano-PCM, this work employs the empirical values presented in [30] for these unknown properties. Motahar et al. [30] experimentally obtained the thermal conductivity of the solid and liquid n-octadecane containing the MPSiO$_2$ particles at different values of mass fraction. They also presented the power-law and consistency indexes of the melted nano-PCM for different values of MPSiO$_2$ particles fraction. Table 1 shows these values. The thermo-physical properties of pure PCM and nanoparticles are also inserted in Table 2. The relations, which give the other properties of the nano-PCM, for the thermo-physical properties of the nano-PCM apply the volume fraction of the nanoparticles. The transition from weight fraction to the volume fraction is done through the following equation:

$$\phi = \frac{\bar{\rho}_{PCM}\phi_{wt}}{\phi_{wt}\bar{\rho}_{PCM} + (1-\phi_{wt})\rho_{np}} \tag{8}$$

It is worth noting that $\bar{\rho}_{PCM}$ of the above equation is the average density of the solid and liquid phases of the host PCM.

The averaged density of the nano-PCM is [34]

$$\rho_{NP} = (1-\phi)\bar{\rho}_{PCM} + \phi\rho_{np} : \bar{\rho}_{PCM} = \left(\rho_{PCM,s} + \rho_{PCM,f}\right)/2 \tag{9}$$

heat capacity of the liquid and solid phases of the nano-PCM is [34]

$$\rho_{NP}C_{p,nf} = \phi\rho_{np}C_{p,np} + (1-\phi)\bar{\rho}_{PCM}C_{p,f} \tag{10a}$$

$$\rho_{NP}C_{p,ns} = \phi\rho_{np}C_{p,np} + (1-\phi)\bar{\rho}_{PCM}C_{p,s} \tag{10b}$$

thermal expansion coefficient of the liquid phase of the nano-PCM is [34]

$$\rho_{NP}\beta_{nf} = (1-\phi)\bar{\rho}_{PCM}\beta_f + \phi\rho_{np}\beta_{np} \tag{11}$$

Latent heat of the nano-PCM can be written as follows [13]

$$(\rho L_h)_{NP} = (1-\phi)\bar{\rho}_{PCM}L_h \tag{12}$$

By defining the following non-dimensional variables

$$\begin{gathered} R = \frac{r}{H},\quad Z = \frac{z}{H},\quad U_R = \frac{u_r H}{\alpha_f},\quad U_Z = \frac{u_z H}{\alpha_f}, \\ \theta = \frac{T - T_{fu}}{T_h - T_{fu}},\quad P = \frac{H^2 p}{\rho\alpha_f^2},\quad Fo = \frac{t\alpha_f}{H^2} \end{gathered} \tag{13}$$

The governing equations are transferred to the non-dimensional form as follows

$$\frac{1}{R}\frac{\partial(RU_R)}{\partial R} + \frac{\partial U_Z}{\partial Z} = 0 \tag{14}$$

$$\begin{aligned} \frac{\partial U_R}{\partial Fo} + U_R\frac{\partial U_R}{\partial R} + U_Z\frac{\partial U_R}{\partial Z} &= -\frac{\bar{\rho}_{PCM}}{\rho_{NP}}\frac{\partial P}{\partial R} \\ &+ \frac{1}{R}\frac{\partial}{\partial R}\left(2PrR\dot{G}^{n_{nf}-1}\left[\frac{m_{nf}}{m_f}\frac{\alpha_f^{n_{nf}}}{\alpha_f^{n_f}}\frac{H^{2n_f}}{H^{2n_{nf}}}\right]\frac{\partial U_R}{\partial R}\right) \\ -2Pr\dot{G}^{n_{nf}-1}\left[\frac{m_{nf}}{m_f}\frac{\alpha_f^{n_{nf}}}{\alpha_f^{n_f}}\frac{H^{2n_f}}{H^{2n_{nf}}}\right]\frac{U_R}{R^2} & \\ &+ \frac{\partial}{\partial Z}\left(Pr\dot{G}^{n_{nf}-1}\left[\frac{m_{nf}}{m_f}\frac{\alpha_f^{n_{nf}}}{\alpha_f^{n_f}}\frac{H^{2n_f}}{H^{2n_{nf}}}\right]\left(\frac{\partial U_R}{\partial Z} + \frac{\partial U_Z}{\partial R}\right)\right) \end{aligned} \tag{15}$$

$$\begin{aligned} \frac{\partial U_Z}{\partial Fo} + U_R\frac{\partial U_Z}{\partial R} + U_Z\frac{\partial U_Z}{\partial Z} &= -\frac{\bar{\rho}_{PCM}}{\rho_{NP}}\frac{\partial P}{\partial z} \\ &+ \frac{1}{R}\frac{\partial}{\partial R}\left(PrR\dot{G}^{n_{nf}-1}\left[\frac{m_{nf}}{m_f}\frac{\alpha_f^{n_{nf}}}{\alpha_f^{n_f}}\frac{H^{2n_f}}{H^{2n_{nf}}}\right]\left(\frac{\partial U_R}{\partial Z} + \frac{\partial U_Z}{\partial R}\right)\right) \\ &+ \frac{\partial}{\partial Z}\left(2Pr\dot{G}^{n_{nf}-1}\left[\frac{m_{nf}}{m_f}\frac{\alpha_f^{n_{nf}}}{\alpha_f^{n_f}}\frac{H^{2n_f}}{H^{2n_{nf}}}\right]\frac{\partial U_Z}{\partial Z}\right) + \frac{\beta_{nf}}{\beta_f}RaPr\theta_{nf} \end{aligned} \tag{16}$$

where

$$\begin{aligned} \dot{G} = 2\left[\left(\frac{\partial U_R}{\partial R}\right)^2 + \left(\frac{U_R}{R}\right)^2 + \left(\frac{\partial U_Z}{\partial Z}\right)^2\right] + \left(\frac{\partial U_R}{\partial Z} + \frac{\partial U_Z}{\partial R}\right)^2 \\ + \left(\frac{\partial U_Z}{\partial R}\right)^2 \end{aligned} \tag{17}$$

$$\begin{aligned} \frac{\partial \theta_{nf}}{\partial Fo} = U_R\frac{\partial \theta_{nf}}{\partial R} + U_Z\frac{\partial \theta_{nf}}{\partial Z} = \frac{\bar{\rho}_{PCM}C_{p,f}}{\rho_{NP}C_{p,nf}}\left(\frac{1}{R}\frac{\partial}{\partial R}\left(\frac{k_{nf}}{k_f}R\frac{\partial \theta_{nf}}{\partial R}\right)\right. \\ \left. + \frac{\partial}{\partial Z}\left(\frac{k_{nf}}{k_f}\frac{\partial \theta_{nf}}{\partial Z}\right)\right) \end{aligned} \tag{18}$$

$$\frac{\rho_{NP}C_{p,ns}}{\bar{\rho}_{PCM}C_{p,f}}\frac{\partial \theta_{ns}}{\partial Fo} = \left(\frac{1}{R}\frac{\partial}{\partial R}\left(\frac{k_{ns}}{k_f}R\frac{\partial \theta_{ns}}{\partial R}\right) + \frac{\partial}{\partial Z}\left(\frac{k_{ns}}{k_f}\frac{\partial \theta_{ns}}{\partial Z}\right)\right) \tag{19}$$

Here Prandtl number (*Pr*) and Rayleigh number (*Ra*) are

$$\begin{aligned} Pr &= \frac{m_f}{\bar{\rho}_{PCM}\alpha_f}\left(\frac{\alpha_f}{H^2}\right)^{n_f-1} = \frac{m_f}{\bar{\rho}_{PCM}}\frac{\alpha_f^{n_f-2}}{H^{2n_f-2}}, \\ Ra &= \frac{\bar{\rho}_{PCM}g\beta_f\left(T_h - T_{fu}\right)H^{2n_f+1}}{m_f\alpha_f^{n_f}} \end{aligned} \tag{20}$$

The velocity components of the forwarding interface boundary in the dimensionless space can be defined as follows

$$U_R = \frac{1}{(1-\phi)}\left[\frac{k_{nf}}{k_f}\frac{\partial \theta_{nf}}{\partial R} - \frac{k_{ns}}{k_f}\frac{\partial \theta_{ns}}{\partial R}\right]Ste \tag{21a}$$

$$U_Z = \frac{1}{(1-\phi)}\left[\frac{k_{nf}}{k_f}\frac{\partial \theta_{nf}}{\partial Z} - \frac{k_{ns}}{k_f}\frac{\partial \theta_{ns}}{\partial Z}\right]Ste \tag{21b}$$

where Stefan number (*Ste*) is

$$Ste = \frac{C_{p,f}(T_h - T_{fu})}{L_h} \tag{22}$$

The boundary and initial conditions at the dimensionless coordinates are

$$\theta = 1,\ U_R = U_Z = 0\quad \forall R,\ Z,\ Fo \mid R = R_i,\ \ 0 \le Z \le 1,\ \ Fo \ge 0 \tag{23a}$$

$$\theta = -0.14,\ U_R = U_Z = 0\quad \forall R,\ Z,\ Fo \mid R = R_o,\ \ 0 \le Z \le 1,\ \ Fo \ge 0 \tag{23b}$$

$$\frac{\partial \theta}{\partial Z} = 0,\ U_R = U_Z = 0\quad \forall R,\ Z,\ Fo \mid Z = 0,\ \ R_i \le R \le R_o,\ \ Fo \ge 0 \tag{23c}$$

$$\frac{\partial \theta}{\partial Z} = 0,\ U_R = U_Z = 0\quad \forall R,\ Z,\ Fo \mid Z = 1,\ \ R_i \le R \le R_o,\ \ Fo \ge 0 \tag{23d}$$

$$\begin{aligned} \theta_0 = \frac{T_0 - T_{fu}}{T_h - T_{fu}},\ U_R = U_Z = 0\quad \forall R,\ Z,\ Fo \mid\ R_i \le R \le R_o,\ \ 0 \le Z \le 1, \\ Fo = 0 \end{aligned} \tag{23e}$$

where $\theta_0 = \theta_c =$ -0.14. Here, the parameters of interest are the volume fraction of melt and the Nusselt number at the hot wall. The volume fraction of melt is normalized respect to the volume of the total space in the cavity. Hence, the normalized melt volume fraction is introduced as

$$NMVF = \frac{\int_0^1\int_{R_i}^{R_m} 2\pi R dRdZ}{\int_0^1\int_{R_i}^{R_o} 2\pi R dRdZ} \tag{24}$$

where the subscript "*m*" denotes the local radius of the moving melting front.

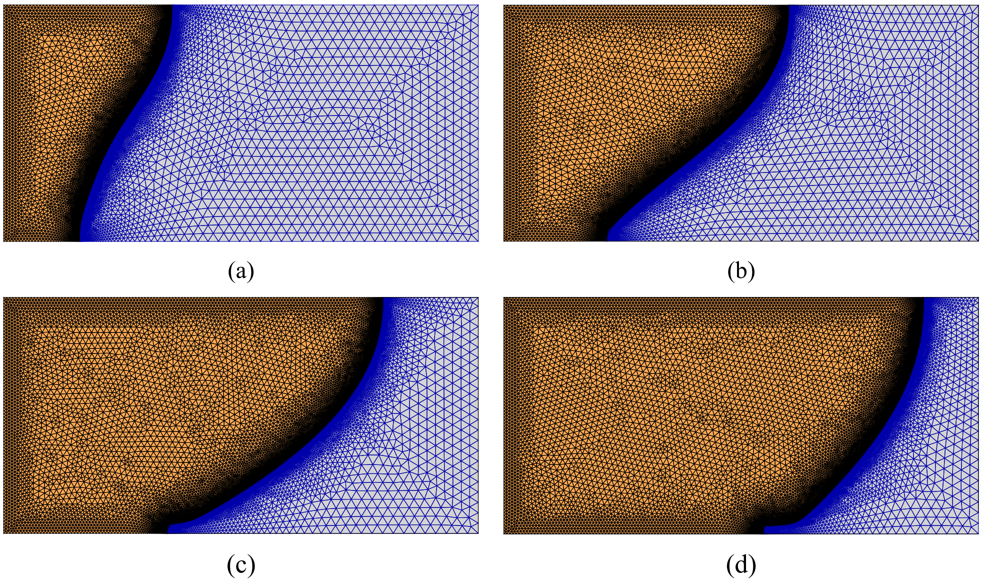
(a) (b) (c) (d)

Fig. 2. Solid (black) and melted (blue) grids for $AR = 0.5$ and different Fourier numbers: (a) $Fo = 1$, (b) $Fo = 2.5$, (c) $Fo = 5$ and (d) $Fo = 10$. (For interpretation of the references to color in this figure legend, the reader is referred to the web version of this article.)

Table 3
Grids of different sizes at required run times.

Case	Number of elements	Number of elements on the solid-liquid interface	Run time
Case 1	4623	130	8 min
Case 2	15,425	190	24 min
Case 3	**42,252**	**350**	**62 min**
Case 4	81,479	420	143 min

Energy balancing of the control surface on the left wall results in the following expression

$$h\left(T_h - T_{fu}\right) = k_{nf}\frac{\partial T}{\partial r}\bigg|_{r = r_0} \tag{25}$$

The transition of the above relation to the non-dimensional coordinates defines local Nusselt number

$$Nu_i = \frac{hH}{k_f} = -\frac{k_{nf}}{k_f}\frac{\partial \theta}{\partial R}\bigg|_{R = R_0} \tag{26}$$

Integrating the local Nusselt number Nu_l along the hot surface, the average Nusselt number Nu_{avg} is evaluates as

$$Nu_{avg} = \int_0^1 Nu_i dZ \tag{27}$$

3. Numerical method, grid examination and validations

The partial differential Eqs. (14)–(19) with the boundary constraints Eqs. (23a)–(23e) are solved by the Galerkin finite element approach. In this method, the PDEs are first transferred to a new form, namely, weak form. The details of the utilized numerical method can be found in [31]. The (Arbitrary Lagrangian–Eulerian) ALE approach is employed for the moving mesh domain. The deformation of the mesh is controlled by the Laplace equation. The motion of mesh at the vertical walls is fixed in R direction, while the motion of horizontal walls is fixed in Z direction. The mesh of the vertical walls is free to move in Z direction, and the mesh of horizontal walls is free to move in R direction. This way, the shape of the enclosure remains intact while the mesh in the domain is allowed to deform along with the interface motion. The motion of the interface is controlled by Eq. (21) in R and Z directions.

The constraint for the continuity equation is introduced as a penalty parameter (γ) in the momentum equations as described by Reddy [31]. In order to complete the numerical calculation, the grid independency of the resolution is studied. Hence, the computations are recalculated for several grid-sizes in the case of $Ra = 8.4 \times 10^5$, $Ste = 0.16$, $Pr = 51.7$, $AR = 0.5$ and $\phi_{wt} = 0.05$. The moving mesh is utilized to solve the problem and the number of elements changes over time (see Fig. 2). The reason for controlling the number of elements at the melting interface is the fact that the motion of the interface is controlled by the energy balance, Eq. (21), and during the interface motions, it can deform severely in some points of the interface. A severe deformation at a point can result in a sharp edge, which has to be handled by a very fine mesh structure and tremendously increase in the local element numbers at the interface. Controlling the interface elements avoids an un-necessary increase in the elements at the interface by maintaining a reasonable fine mesh interface.

Table 3 demonstrates the utilized final grids-sizes. The melting interface, melted volume fraction and the average Nusselt number on the inner wall are depicted in Figs. 3–5, as a function of time for different grid sizes. The results show that the grid size of case 3 can provide acceptable accuracy and with an increase in the number of the elements, the results of case 3 become almost independent from the element number. Therefore, the grid size of case 3 is selected to carry out the results of the present study, and the adopted case 3 is indicated as bold in Table 3.

The correctness and accuracy of the numerical outcomes can be verified and validated through the other numerical and experimental results, reported in [26–28]. As a verification of the natural convection inside a vertical coaxial pipe, Kumar and Kalam's investigation [26] has been studied. In Kumar and Kalam's work [26], the inner pipe maintained at a higher temperature compared to the outer one, and the bottom and upper walls were perfectly

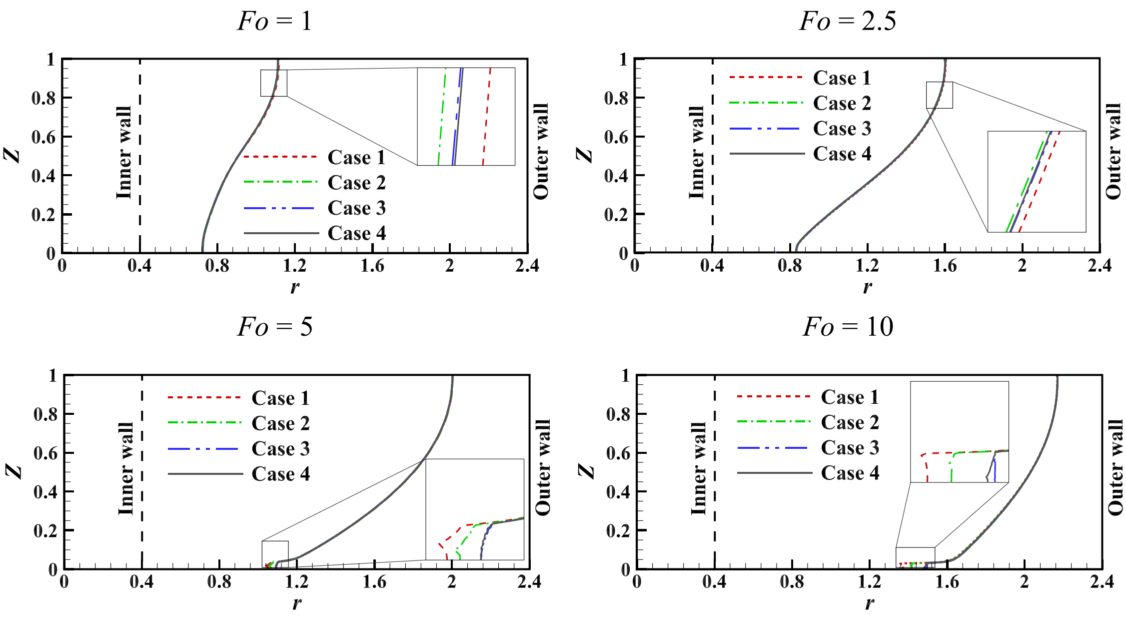

Fig. 3. Development of melting frontier with passing the non-dimensional time ($AR = 0.5$, $\phi_{wt} = 0.05$) for Cases 1–4

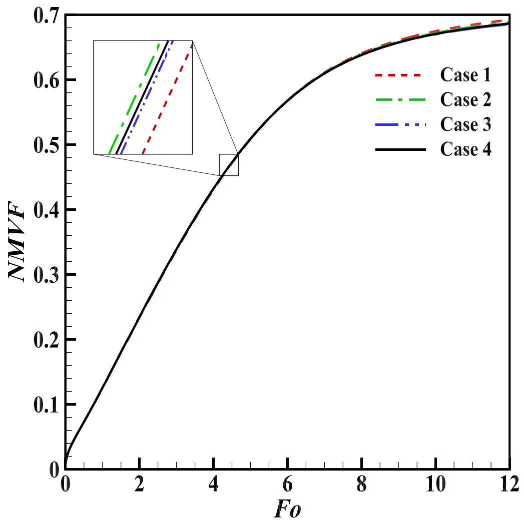

Fig. 4. The fraction of melted PCM with passing the non-dimensional time ($AR = 0.05$, $\phi_{wt} = 0.05$) for Cases 1–4.

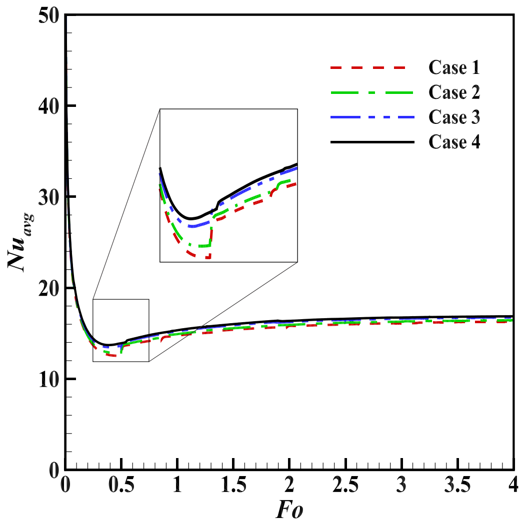

Fig. 5. Average Nusselt number with passing the non-dimensional time ($AR = 0.05$, $\phi_{wt} = 0.05$) for Cases 1–4.

insulated. The space between the outer and inner pipes was occupied with air as a Newtonian fluid. Fig. 6 shows a comparison of the outcomes of the present study with the outcomes of Kumar and Kalam's study [26]. The constant parameters for this evaluation are $Pr = 0.71$, $L/(r_o{-}r_i) = 1$. The comparison shows that there is a desirable agreement between the results.

To verify the natural convection of a non-Newtonian power-law fluid in an enclosure, the study of Matin and Khan [37] is re-simulated through the utilized code in the present study. Matin and Khan [37] studied the free convective heat transfer of a non-Newtonian power-law fluid in an annuli of the horizontal cylinders with the hot and cold temperatures at the inner and outer cylinders. For a case of non-Newtonian fluid with $Pr = 10$ and $Ra = 10^3$, a comparison between the average Nusselt numbers of the present study and those of [37] is displayed in Fig. 7 for different values of the power-law index. As shown, the results are in excellent agreement.

For validation and verification of the melting process, comparisons between the melting fronts obtained in the present study and those presented in [38] are conducted, as depicted in Fig. 8. The problem physics studied in [38] included a square cavity with the horizontal insulated walls. However, the left and right borders of the cavity are subjected to high and low temperatures. The pure gallium was selected as the Newtonian phase change substance. The dimensionless parameters based on the thermo-physical properties of the PCM, the thermal boundary conditions, and the geometrical characteristics were such that $Pr = 0.0216$, $Ra = 6 \times 10^5$, and $Ste = 0.039$. As shown in Fig. 8, the results of the current work are in good agreement with data of Gau and Viskanta [38]. As the comparisons conducted in Figs. 6–8 demonstrate that the numerical modeling has correctly been performed and the utilized code is reliable.

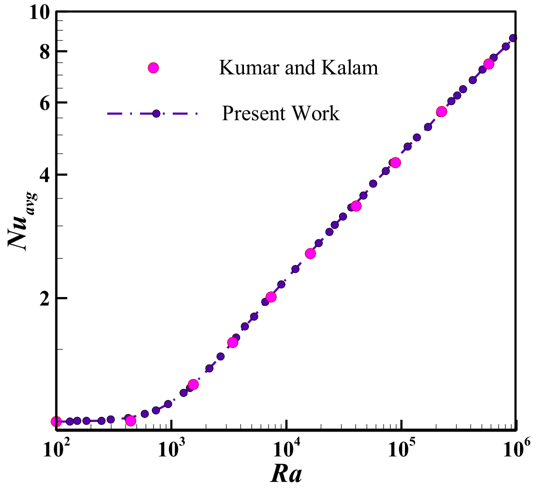

Fig. 6. Average Nusselt number against Rayleigh number of the current study (dash-dot) and Kumar et al. [32] (points).

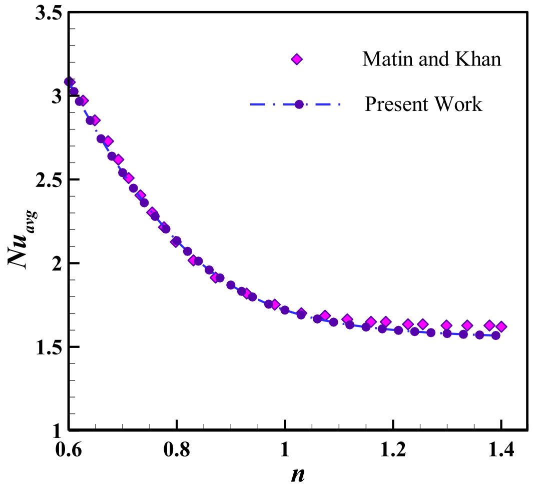

Fig. 7. Average Nusselt number against power-law index n of the current study (dash-dot) and Matin and Khan [37] (points).

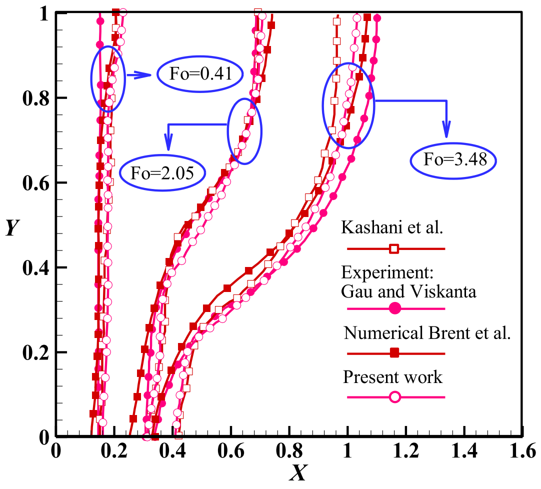

Fig. 8. Comparison between the melting front obtained by the current work and reported in [38].

4. Results and discussion

In this section, a natural convection study of the melting process of a PCM with MPSiO$_2$ nanoparticles and non-Newtonian effects in a coaxial pipe is numerically conducted. The height of the pipe, as a constraint, is considered to be 12.5 mm. The temperatures of the hot and cold surfaces are set at $T_h = 45^\circ\text{C}$ and $T_c = 25^\circ\text{C}$. Also, the melting point is obtained to be 27.5°C. For the considered coaxial pipe and the thermophysical properties of the base PCM, $Ra = 8.4 \times 10^5$, $Ste = 0.16$, $AR = 0.5$, $\phi_{wt} = 0.05$, and $Pr = 51.7$ are adopted as the default values of non-dimensional parameters. The results are reported for the set of the default values of non-dimensional parameters; otherwise, the value of the parameter will be stated. In this work, the effects of dispersing MPSiO$_2$ particles in the PCM and the aspect ratio ($0.5 \leq AR \leq 2$) on the melting process are investigated.

Fig. 9 illustrates the isotherms and streamlines in the enclosure with an aspect ratio of $AR = 0.5$ for various values of solid particles concentration. The corresponding melting interfaces, melting volume fraction, and average Nusselt numbers are depicted in Figs. 10, 11, and 12, respectively. The contours for very low Fourier numbers are not depicted here, but our computations showed that the velocity field is very weak, and the melting frontier is almost vertical and parallel to the inner wall in very low Fourier numbers (less than 0.01). In this case, the convection term in Eqs. (15) and (16) is negligible. During this period of non-dimensional time, the temperature gradient along the Z-direction is almost negligible, so the movement of the melting frontier along Z-direction is almost zero. Moreover, a detailed study of the numeric computations revealed that the temperature gradients along the radial direction in the melted zone are stronger than that of the solid section revealed that, as the solid section absorbs the heat by latent heat while the liquid received the heat in the form of sensible heat. Therefore, according to Eq. (21), the increase in the volume fraction of nanoparticles tends to increase in the moving velocity of the melting frontier. This increase in the velocity is due to two reasons. The first reason is the fact that the nanoparticles do not contribute to latent heat storage/release, and hence, the increase in the volume fraction of nanoparticles reduces the amount of PCM. This effect is attributed to the term of $(1-\phi)$ in Eq. (21). The second reason is the improvement of thermal conductivity of the mixture which improves the heat transfer and accelerates the movement of the melting frontier. However, as depicted in Fig. 9, the melting front advances by the increase of Fourier numbers. In this case, the buoyancy forces induce a critical non-linear effect that can change the temperature gradients and the moving behavior of the melting frontier.

Besides, with increasing the mass fraction of nanoparticles the thermal conductivity is improved, and hence, at the early stage of the melting process, which is a conduction dominant heat transfer, the heat transfer rate (the Nusselt number) increases. At $Fo = 0.01$, Nusselt number was computed as 38.18, 38.5, 39.08 and 39.4, for 0%, 1%, 3% and 5% mass fraction of nanoparticles, respectively.

However, as depicted in Fig. 9, the melting front advances by the increase of Fourier numbers. In this case, the buoyancy forces induce a critical non-linear effect that can change the temperature gradients and the moving behavior of the melting frontier. For all mass fractions, Fig. 9 shows that the temperature gradient in the melted zone decreases over time due to the low velocity of the fluid field as well as the increased thickness of the molten layer, which in turn decreases the Nusselt number (see Fig. 12). Just after the early stages of the melting heat transfer, both the conduction and natural convection heat transfer mechanisms are weak. About $Fo = 0.1$–0.5, the Nusselt number increases for all mass fractions. This is since the velocity field of the fluid in the melted zone in-

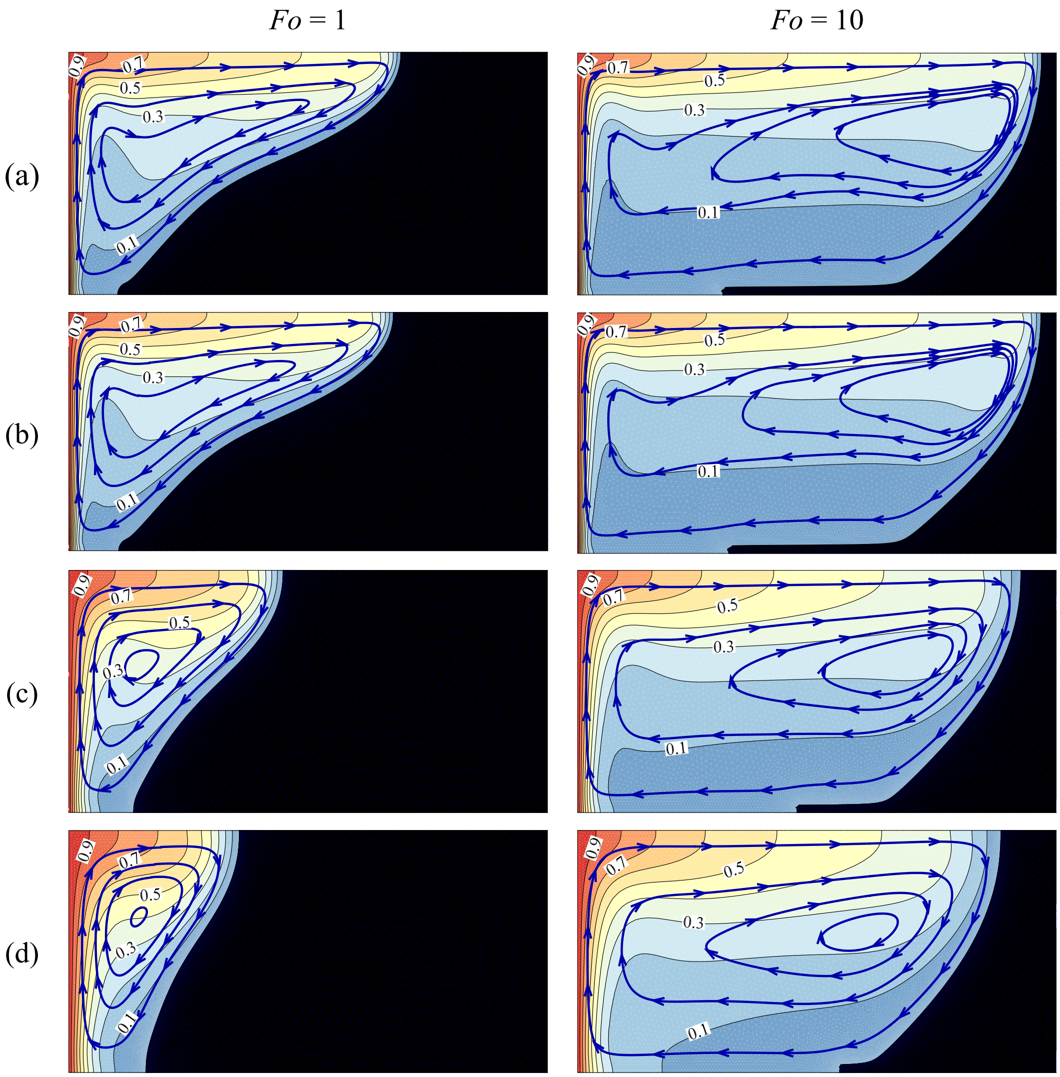

Fig. 9. Development of isothermal contours and streamlines: (a) $\phi_{wt} = 0.00$, (b) $\phi_{wt} = 0.01$, (c) $\phi_{wt} = 0.03$, (d) $\phi_{wt} = 0.05$ inside melted NePCM for $AR = 0.5$ with passing non-dimensional time.

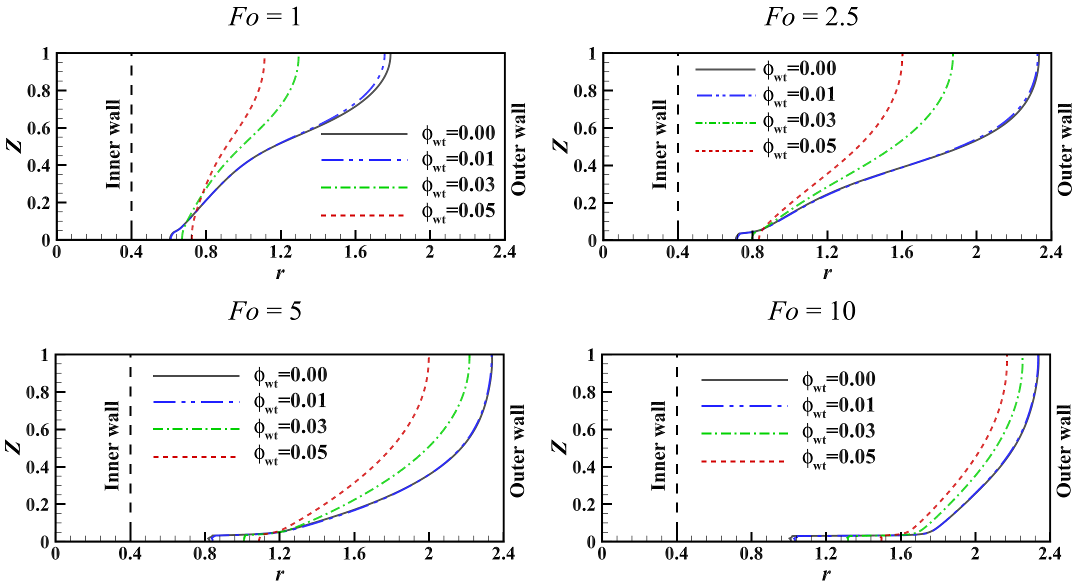

Fig. 10. Development of melting frontier with passing non-dimensional time for different mass fraction and $AR = 0.5$.

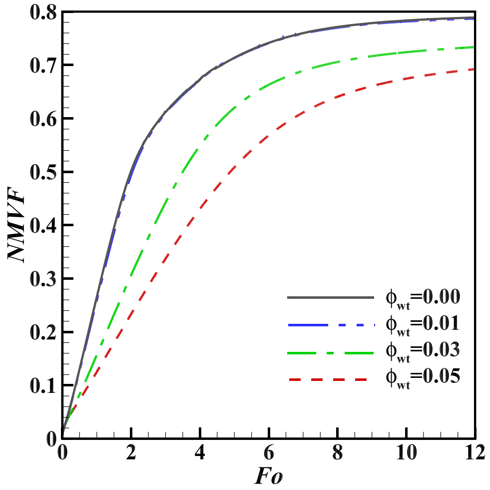

Fig. 11. The fraction of melted PCM with passing non-dimensional time for different mass fraction and $AR = 0.5$.

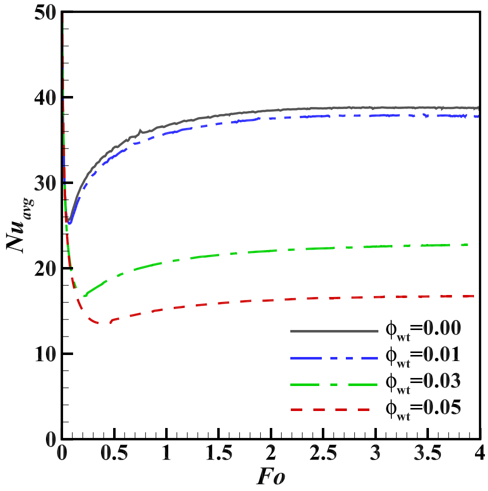

Fig. 12. Average Nusselt number with passing non-dimensional time for different mass fraction and $AR = 0.5$.

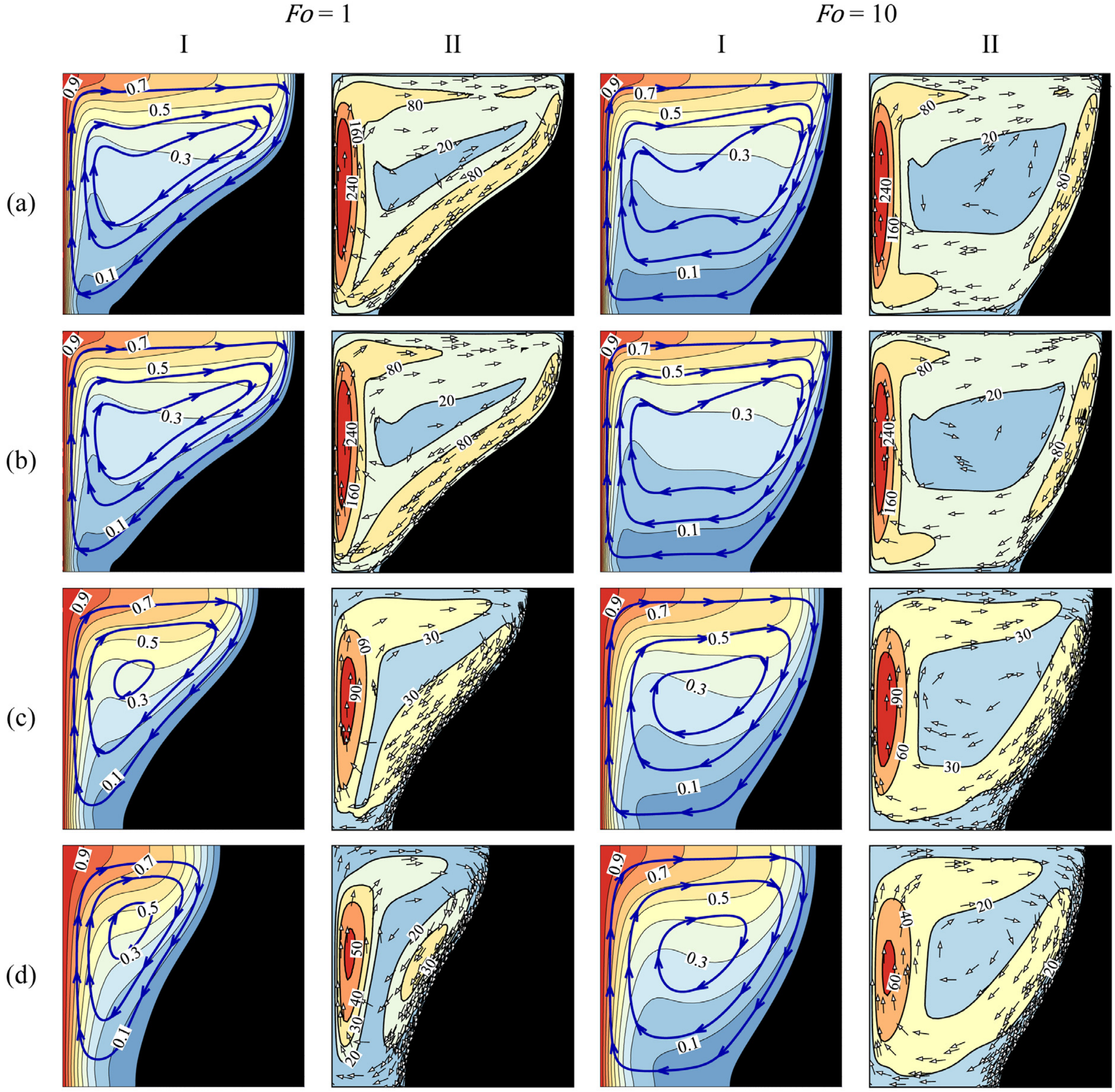

Fig. 13. Development of (I) isotherms and streamlines and (II) velocity vectors and velocity magnitude contours: (a) $\phi_{wt} = 0.00$, (b) $\phi_{wt} = 0.01$, (c) $\phi_{wt} = 0.03$, (d) $\phi_{wt} = 0.05$ inside melted NePCM concerning $AR = 1$ with passing non-dimensional time.

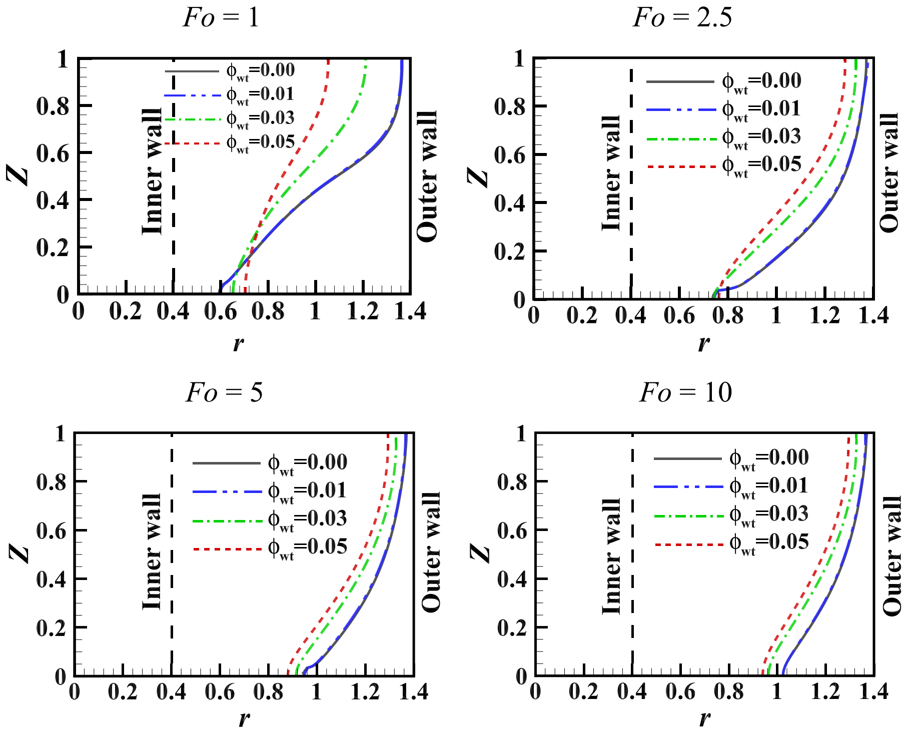

Fig. 14. Development of melting frontier with passing non-dimensional time for different mass fraction and $AR = 1$.

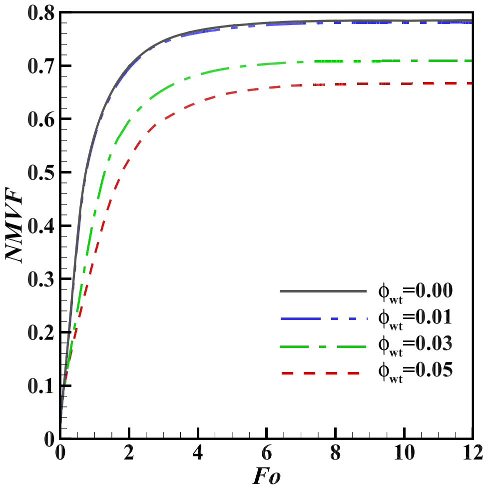

Fig. 15. The fraction of melted PCM with passing non-dimensional time for different mass fraction and $AR = 1$.

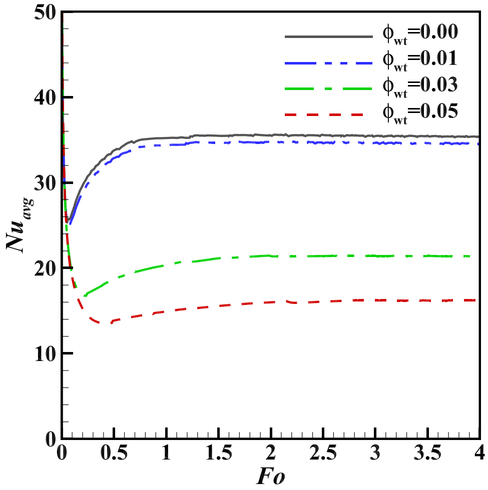

Fig. 16. Average Nusselt number with non-dimensional time for different mass fractions and $AR = 1$.

creases over time gradually, and it leads to increase in the temperature gradient near the inner wall.

After $Fo = 0.01$, the buoyancy forces get important, and the molten region starts weak circulation flows. Increasing the mass fraction reduces the velocity field. As the velocity field of the fluid decreases, the convection term of the energy equation (Eq. (18)) drops. Therefore, it can be considered that increasing the mass fraction results in reducing the thermal heat flux on the inner wall (decreasing the Nusselt number) and this decreases the melted volume fraction (see Fig. 11).

Also, according to increasing mass fraction and decreasing velocity field, temperature gradient decreases in the melted zone, but it is expected that the increasing the mass fraction provides a minor effect on the temperature gradient in the solid zone in comparison with the melted zone due to the lack of convection term in energy equation (Eq. 19) and the barrier of fusion heat transfer at the melting frontier. Increasing the mass fraction also leads to an increase in the volume fraction and $1/(1-\phi)$ coefficient in Eq. (21), but in the case of convective heat transfer this increase is overridden by the effect of buoyancy forces and convective circulations in the enclosure. It should be noted that increasing the mass fraction by 5% only causes 1% change in the coefficient $1/(1-\phi)$. Therefore, it could be considered that increasing the mass fraction leads to a decrease in the non-Newtonian power-law index (Table 1) as well as the velocity of melting frontier (see Eq. (21) and Fig. 10). Also, Fig. 11 shows that increasing the mass fraction results in a decrease in the melting rate of nano-enhanced PCM.

For the Fourier number between 3 and 5, the value of Nusselt number remains constant for all mass fractions (see Fig. 12), due to

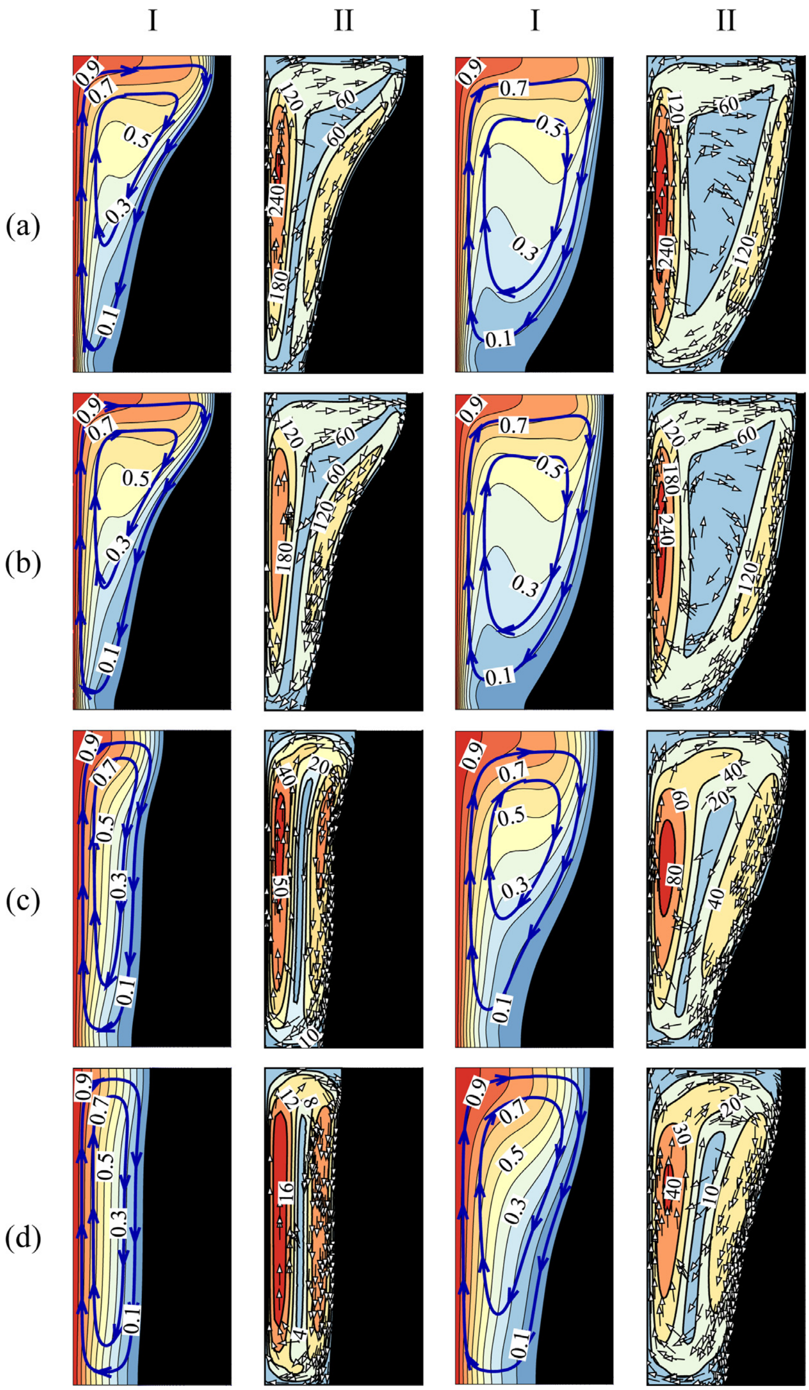

Fig. 17. Development of (I) isotherms and streamlines and (II) velocity vectors and velocity magnitude contours: (a) $\phi_{wt} = 0.00$, (b) $\phi_{wt} = 0.01$, (c) $\phi_{wt} = 0.03$, (d) $\phi_{wt} = 0.05$ inside melted NePCM concerning $AR = 2$ with passing non-dimensional time.

the equivalence between the convection and diffusion terms of the energy Eq. (18). In this range of Fourier numbers, the variation of temperature field over time will be negligible for all mass fractions, especially near the inner wall (see Fig. 9). So, the heat flux of the inner wall and Nusselt number do not change over time.

For the Fourier number between 10 and 12, the velocity of the melting frontier tends to zero and the melted volume fraction experiences no changes over time (Figs. 9–11) for all mass fractions. Since that according to Eq. (21), the inlet heat flux from the inner wall to the melted zone is equal to the outlet heat flux from the melted zone to the solid portion, and these two terms are balanced. Due to the effect of the addition of nano-particles on the melting behavior of PCM, the final melted volume fraction will be lower for higher mass fractions.

In general, it can be concluded that the melting behavior of non-Newtonian nano-enhanced PCM is mostly affected by the mass fraction of nanoparticles. It should be noted that according to the experimental data, the non-Newtonian power-law indexes for both 0% and 1% mass fraction are equal to 1, the results of these two mass fractions are close together.

At initial times, the distance between the inner wall and the melting front is small, so the conduction mechanism is dominant. In this case, due to the thinness of the molten layer, the temperature profile from the inner wall to the melting front experiences a

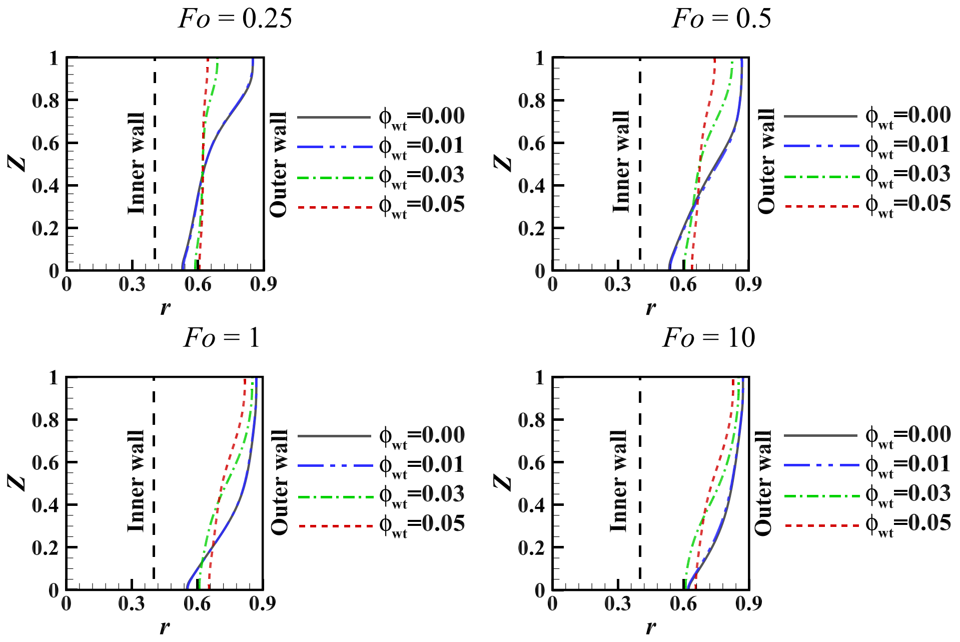

Fig. 18. Development of melting frontier with passing non-dimensional time for different mass fraction and $AR = 2$.

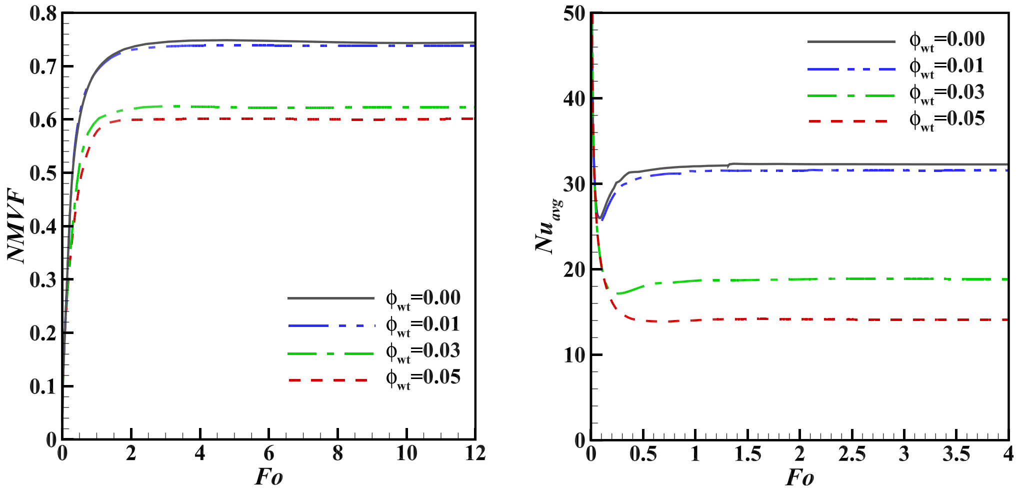

(a) (b)

Fig. 19. The fraction of melted PCM (a) and average Nusselt number (b) with passing non-dimensional time for different mass fraction and $AR = 2$.

high gradient, that is why in the initial times the Nusselt number is significantly high. Continuing with the melt front, the temperature gradient decreases, resulting in a decrease in Nusselt number. Also, with the advance of the melting front, the free convection is gradually strengthened, and as a result, the heat transfer is increased until it reaches a constant value.

The phase change behavior is also investigated for $AR = 1$ in Figs. 13–16 and $AR = 2$ in Figs. 17–20 to explore the effects of the mass fraction on the melting behavior of the PCM in these two aspect ratios. According to Figs. 13 and 14, most changes in temperature contours, streamlines, and the location of melting frontier (for $AR = 1$) occur for $Fo < 5$. Figs. 18 and 19 also show that the melting frontier displacement occurs for $Fo < 1$ at $AR = 2$, generally. The reason is that there is always a solid layer attached to the outer wall (due to lower temperature of the outer wall than the melting temperature) which limits the advancement of the melting frontier and final melted volume fraction. The higher the aspect ratio, the greater the coaxial tube thickness, and hence, the melting frontier reaches its final limit faster. Also, according to Figs. 9, 13, 17 for all three aspect ratios, the most melted volume is from the upper part of the PCM due to the higher temperature and heat flux of the upper half of the geometry. The velocity magnitude and velocity vectors are also plotted in Figs. 13 and 17 to show the natural convection flow dynamic in the liquid region. The highest velocity magnitudes are in the vicinity of the hot wall, while the velocity magnitudes next to the melting interface are moderate. This is due to the larger surface area of the melting interface compared to the hot wall. The surface area of the hot wall is smaller than the surface area of the melting interface. Hence, there is the stronger temperature gradient and stronger flow convection at the hot wall compared to the cold melting interface. The number of the velocity vectors is higher next to the melting interface which is due to the higher mesh resolution in this part of the domain of solution.

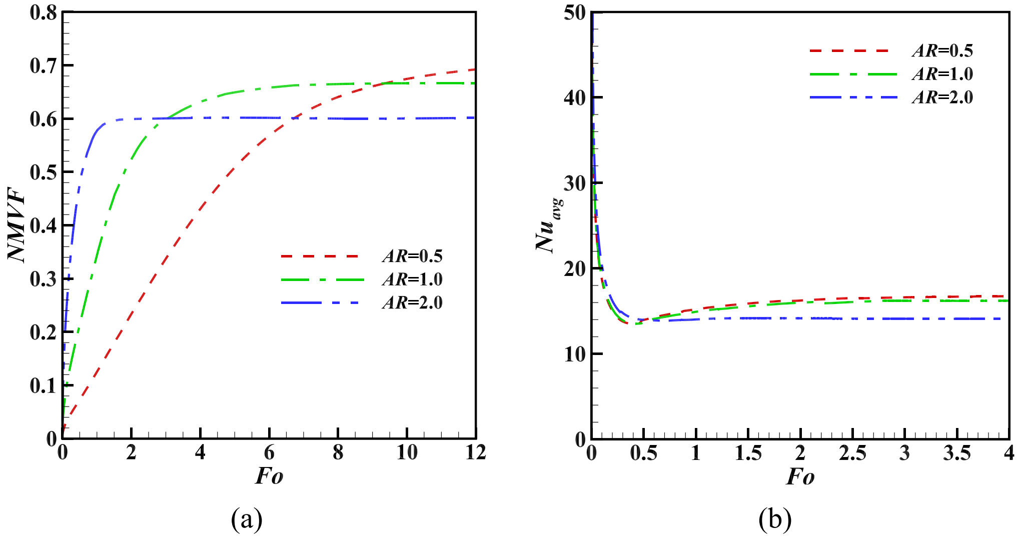

Fig. 20. The fraction of melted PCM (a) and average Nusselt number (b) with passing non-dimensional time for different aspect ratio and $\phi_{wt} = 0.05$.

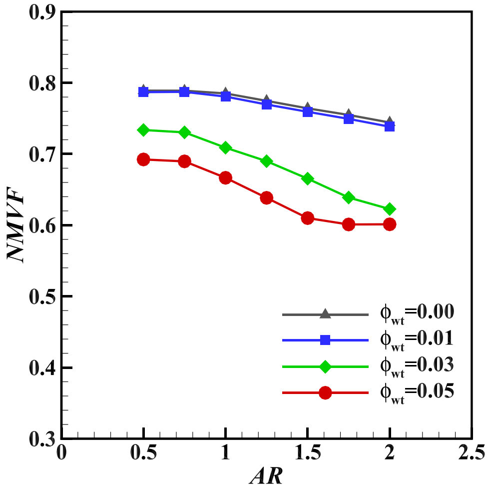

Fig. 21. Final fraction of melted PCM for different aspect ratios between 0.5 and 2.5 and different mass fractions (Maximum $Fo = 12$).

As mentioned before, the experimental data shows that increasing the mass fraction of the nanoparticles reduces the non-Newtonian power-law index. Also, due to the weakness of the momentum convection, the diffusion term in momentum Eq. (15) and (16) is dominant. Increasing the mass fraction of the nanoparticles, which decreases the thermal convection. Therefore, it can be concluded that increasing the mass fraction for all aspect ratios leads to a decrease in the heat flux to the inner wall and the Nusselt number (Figs. 16 and 19b) and also a decrease in the melted volume fraction (Figs. 15 and 19a).

Fig. 20a and b show the melted volume fraction and the average Nusselt number for the three aspect ratios of 0.5, 1 and 2, respectively. According to these figures, the melting rate is fast for higher aspect ratios at low Fourier numbers, and the melted volume fraction and average Nusselt number reach their final limit faster. The higher aspect ratio, the lower coaxial tube thickness and the lower melting frontier distance from its limit, so the heat transfer reaches its steady-state faster. According to Fig. 20a and b in a steady-state, as the aspect ratio increases, the average Nusselt number, and final melted volume fraction are decreased. Since the higher aspect ratio, the less space available for the formation of eddies and free convection heat transfer, and it leads to a lower final average Nusselt number and final melted volume fraction.

The calculations of the melting process are also performed for various aspect ratios (*AR*) in the range of 0.5 to 2 with 0.25 step sizes, and the final melted volume fraction for the mass fraction of 0.00, 0.01, 0.03 and 0.05 is presented in Fig. 21. As discussed earlier, the final melted volume fraction decreases by increasing the aspect ratio for all mass fractions. Also, by increasing the mass fraction of the nanoparticles, the flow circulation, and free convection heat transfer are decreased, and it leads to a decrease in the final melted volume fraction.

5. Conclusion

In the present study, the melting heat transfer of a power-law non-Newtonian nano-enhanced PCM in a gap between isothermal vertical cylinders was studied. The inner cylinder was kept at high temperature, while the outer one was kept at low temperature. The governing equations were introduced in the unsteady form to study the melting process. Then, the governing equations were reduced into a dimensionless form to generalize the outcomes. The finite element method was employed. The grid check analysis and validation studies were performed to ensure the accuracy of the results. The impacts of nanoparticles volume fraction and cylinder aspect ratio on melt flow, heat transfer, average Nusselt number, and melted PCM fraction were investigated.

The addition of nanoparticles leads to a reduction of the melting intensity due to the growth of the material viscosity. As a result, the average Nusselt number is a decreasing function of nanoparticle volume fraction. The rise of the cavity aspect ratio characterizes a more intensive melting due to the growth of the temperature gradients. The average Nusselt number and fraction of melted PCM are reduced with the aspect ratio.

Declaration of competing interest

The authors clarify that there is no conflict of interest for report.

Supplementary materials

Supplementary material associated with this article can be found, in the online version, at doi:10.1016/j.ijheatmasstransfer.2020.119385.

CRediT authorship contribution statement

S.A.M. Mehryan: Conceptualization, Methodology, Software, Validation, Data curation. **Mohammad Vaezi:** Visualization, Software, Investigation, Formal analysis, Data curation. **Mikhail Sheremet:** Conceptualization, Writing - review & editing. **Mohammad Ghalambaz:** Conceptualization, Methodology, Validation, Data curation, Writing - original draft, Supervision, Project administration, Writing - review & editing.

References

[1] Z. Khattak, H.M Ali, Air cooled heat sink geometries subjected to forced flow: a critical review, Int. J. Heat Mass Trans. 130 (2019) 141–161.
[2] S.K. Sahoo, M.K. Das, P. Rath, Application of TCE-PCM based heat sinks for cooling of electronic components: a review, Renew. Sustain. Energy Rev. 59 (2016) 550–582.
[3] P.K.S. Rathore, S.K. Shukla, Potential of macroencapsulated pcm for thermal energy storage in buildings: a comprehensive review, Constr. Build. Mater. 225 (2019) 723–744.
[4] M. Dardir, K. Panchabikesan, F. Haghighat, M. El Mankibi, Y. Yuan, Opportunities and challenges of PCM-to-air heat exchangers (PAHXs) for building free cooling applications—a comprehensive review, J. Energy Storage 22 (2019) 157–175.
[5] J. Jaguemont, N. Omar, P. Van den Bossche, J. Mierlo, Phase-change materials (PCM) for automotive applications: a review, Appl. Therm. Eng. 132 (2018) 308–320.
[6] M. Al-Maghalseh, K. Mahkamov, Methods of heat transfer intensification in PCM thermal storage systems, Renew. Sustain. Energy Rev. 92 (2018) 62–94.
[7] L. Jiang, H. Zhang, J. Li, P. Xia, Thermal performance of a cylindrical battery module impregnated with PCM composite based on thermoelectric cooling, Energy (2019) 116048.
[8] T. Bouhal, T. Kousksou, A. Jamil, CFD thermal energy storage enhancement of PCM filling a cylindrical cavity equipped with submerged heating sources, J. Energy Storage 18 (2018) 360–370.
[9] Y.T. Lee, M.H. Kim, S.S. Lee, J. Gim, J.D. Chung, Numerical analysis in a full-scale thermal energy storage tank with dual PCM capsules, Energy Build. (2019) 109410.
[10] M. Bechiri, K. Mansouri, Study of heat and fluid flow during melting of PCM inside vertical cylindrical tube, Int. J. Therm. Sci. 135 (2019) 235–246.
[11] H. Behi, M. Ghanbarpour, M. Behi, Investigation of PCM-assisted heat pipe for electronic cooling, Appl. Therm. Eng. 127 (2017) 1132–1142.
[12] F. Iachachene, Z. Haddad, H.F. Oztop, E. Abu-Nada, Melting of phase change materials in a trapezoidal cavity: Orientation and nanoparticles effects, J. Molec. Liquids (2019).
[13] M. Ghalambaz, S.H. Zadeh, S. Mehryan, I. Pop, D. Wen, Analysis of melting behavior of PCMs in a cavity subject to a line source magnetic field using a moving grid technique, Appl. Math. Model. (2019).
[14] N.S. Bondareva, M.A. Sheremet, Effect of inclined magnetic field on natural convection melting in a square cavity with a local heat source, J. Magnet. Magnet. Mater. 419 (2016) 476–484.
[15] N.S. Bondareva, M.A. Sheremet, Natural convection heat transfer combined with melting process in a cubical cavity under the effects of uniform inclined magnetic field and local heat source, Int. J. Heat Mass Trans. 108 (2017) 1057–1067.
[16] N.S. Bondareva, M.A. Sheremet, 3D natural convection melting in a cubical cavity with a heat source, Int. J. Ther. Sci. 115 (2017) 43–53.
[17] N.S. Bondareva, M.A. Sheremet, Flow and heat transfer evolution of PCM due to natural convection melting in a square cavity with a local heater, Int. J. Mech. Sci. 134 (2017) 610–619.
[18] N.S. Bondareva, M.A. Sheremet, Conjugate heat transfer in the PCM-based heat storage system with finned copper profile: application in electronics cooling, Int. J. Heat Mass Trans. 124 (2018) 1275–1284.
[19] A. Shenoy, M. Sheremet, I. Pop, Convective Flow and Heat Transfer From Wavy Surfaces: Viscous Fluids, Porous Media, and Nanofluids, CRC Press, 2016.
[20] R. Mohebbi, M. Rashidi, Numerical simulation of natural convection heat transfer of a nanofluid in an L-shaped enclosure with a heating obstacle, J. Taiwan Inst. Chem. Eng. 72 (2017) 70–84.
[21] R. Mohebbi, M. Rashidi, M. Izadi, N.A.C. Sidik, H.W. Xian, Forced convection of nanofluids in an extended surfaces channel using lattice Boltzmann method, Int. J. Heat Mass Trans. 117 (2018) 1291–1303.
[22] R. Mohebbi, M. Izadi, A.J. Chamkha, Heat source location and natural convection in a C-shaped enclosure saturated by a nanofluid, Phy. Fluids 29 (12) (2017) 122009.
[23] Y. Ma, R. Mohebbi, M.M. Rashidi, Z. Yang, Effect of hot obstacle position on natural convection heat transfer of MWCNTs-water nanofluid in U-shaped enclosure using lattice Boltzmann method, Int. J. Num. Methods Heat Fluid Flow 29 (1) (2019) 223–250.
[24] M. Izadi, R. Mohebbi, A. Chamkha, I. Pop, Effects of cavity and heat source aspect ratios on natural convection of a nanofluid in a C-shaped cavity using lattice Boltzmann method, Int. J. Num. Methods Heat Fluid Flow 28 (8) (2018) 1930–1955.
[25] M. Izadi, R. Mohebbi, A.A. Delouei, H. Sajjadi, Natural convection of a magnetizable hybrid nanofluid inside a porous enclosure subjected to two variable magnetic fields, Int. J. Mech. Sci. 151 (2019) 154–169.
[26] M. Ghalambaz, A. Doostani, A.J. Chamkha, M.A. Ismael, Melting of nanoparticles-enhanced phase-change materials in an enclosure: effect of hybrid nanoparticles, Int. J. Mech. Sci. 134 (2017) 85–97.
[27] A. Chamkha, A. Doostanidezfuli, E. Izadpanahi, M. Ghalambaz, Phase-change heat transfer of single/hybrid nanoparticles-enhanced phase-change materials over a heated horizontal cylinder confined in a square cavity, Adv. Powder Technol. 28 (2) (2017) 385–397.
[28] M. Ghalambaz, A.J. Chamkha, D. Wen, Natural convective flow and heat transfer of Nano-Encapsulated Phase Change Materials (NEPCMs) in a cavity, Int. J. Heat Mass Trans. 138 (2019) 738–749.
[29] M. Ghalambaz, T. Groşan, I. Pop, Mixed convection boundary layer flow and heat transfer over a vertical plate embedded in a porous medium filled with a suspension of nano-encapsulated phase change materials, J. Molec. Liquids 293 (2019) 111432.
[30] S. Motahar, N. Nikkam, A.A. Alemrajabi, R. Khodabandeh, M.S. Toprak, M. Muhammed, A novel phase change material containing mesoporous silica nanoparticles for thermal storage: a study on thermal conductivity and viscosity, Int. Commun. Heat Mass Trans. 56 (2014) 114–120.
[31] J.N. Reddy, An Introduction to the Finite Element Method, 1993 New York.
[32] R. Kumar, M. Kalam, Laminar thermal convection between vertical coaxial isothermal cylinders, Int. J. Heat Mass Trans. 34 (2) (1991) 513–524.
[33] N. Zeraibi, M. Amoura, A. Benzaoui, M. Gareche, Numerical study of a thermodependent non-Newtonian fluid flow between vertical concentric cylinders, Int. Commun. Heat Mass Trans. 34 (6) (2007) 740–752.
[34] M. Izadi, M.A. Sheremet, S. Mehryan, I. Pop, H.F. Öztop, N. Abu-Hamdeh, MHD thermogravitational convection and thermal radiation of a micropolar nanoliquid in a porous chamber, Int. Commun. Heat Mass Trans. 110 (2020) 104409.
[35] N.H. Boukani, A. Dadvand, A.J. Chamkha, Melting of a Nano-enhanced Phase Change Material (NePCM) in partially-filled horizontal elliptical capsules with different aspect ratios, Int. J. Mech. Sci. 149 (2018) 164–177.
[36] M. Jahanshahi, S. Hosseinizadeh, M. Alipanah, A. Dehghani, G. Vakilinejad, Numerical simulation of free convection based on experimental measured conductivity in a square cavity using Water/SiO2 nanofluid, Int. Commun. Heat Mass Trans. 37 (6) (2010) 687–694.
[37] M.H. Matin, W.A. Khan, Laminar natural convection of non-Newtonian power-law fluids between concentric circular cylinders, Int. Commun. Heat Mass Trans. 43 (2013) 112–121.
[38] C. Gau, R. Viskanta, Melting and solidification of a pure metal on a vertical wall, J. Heat Trans. 108 (1) (1986) 174–181.